# Semiannual Technical Summary

## Integrated Optical Circuits

31 December 1973

Prepared for the Advanced Research Projects Agency
under Electronic Systems Division Contract F19628-73-C-0002 by

# Lincoln Laboratory

MASSACHUSETTS INSTITUTE OF TECHNOLOGY

LEXINGTON, MASSACHUSETTS

This technical report has been reviewed and is approved for publication.

FOR THE COMMANDER

Eugene C. Raabe, Lt. Col., USAF
Chief, ESD Lincoln Laboratory Project Office

MASSACHUSETTS INSTITUTE OF TECHNOLOGY

LINCOLN LABORATORY

# INTEGRATED OPTICAL CIRCUITS

SEMIANNUAL TECHNICAL SUMMARY REPORT
TO THE
ADVANCED RESEARCH PROJECTS AGENCY

1 JULY – 31 DECEMBER 1973*

ISSUED 31 MAY 1974

---

* Period covered in first semiannual was incorrect (31 July cited instead of 30 June).

LEXINGTON                                         MASSACHUSETTS

## ABSTRACT

$In_xGa_{1-x}As$ avalanche photodiodes have been integrated into GaAs waveguide structures by selective epitaxial deposition. The planar waveguides which were fabricated by growing high-purity $(10^{14} \text{ cm}^{-3})$ epitaxial layers on heavily doped $(10^{18} \text{ cm}^{-3})$ substrates had losses of less than 1 dB/cm at 1.06 μm. Integrated monolithic $In_{0.2}Ga_{0.8}As$ Schottky barrier avalanche photodiodes operated as waveguide detectors had quantum efficiencies of 60 percent and current gains of about 50 at 1.06 μm. Measurements of the ionization coefficients of electrons ($\alpha$) and holes ($\beta$) have been made for GaAs by using a special type of GaAs Schottky barrier avalanche photodiode structure. The results show that, contrary to the previously accepted belief, $\alpha$ and $\beta$ are not equal but that $\beta > \alpha$. This inequality is favorable for achieving high gain-bandwidth products and low excess noise in GaAs avalanche photodiodes. A new type of GaAs avalanche photodiode which has considerable advantages for detection at wavelengths up to about 0.93 μm has been investigated. This device, which has been named electroabsorption avalanche photodiode (EAP), depends on the Franz-Keldysh shift of the band edge to cause sufficient absorption in the 0.90- to 0.93-μm wavelength range.

Significant progress has been made in the vapor epitaxial growth of $Hg_{1-x}Cd_xTe$ and CdTe substrates by $H_2$ transport. Single crystal layers of $Hg_{1-x}Cd_xTe$ have been grown over the alloy composition range from x = 0 to x = 0.98. The layers appear to be of good crystal quality and have Hall mobility values comparable to those observed in bulk material of similar composition. High-energy proton bombardment has been used to fabricate waveguides for 10.6 μm in CdTe. The attenuation has been measured for different thickness waveguides and found to be in good agreement with calculated attenuation due to free-carrier absorption in the substrate. Attenuation as low as 1 dB/cm has been measured in 37-μm-thick waveguides. Coupling of 10.6-μm radiation into CdTe waveguides has been explored (1) by focusing a $CO_2$ laser beam onto a cleaved end face of a waveguide structure, and (2) by using grating couplers which were sputter-etched in the top surface of the waveguide. A coupling efficiency of about 70 percent was achieved with end-face coupling and a maximum of 15 percent with grating couplers. The feasibility of integrated surface acoustic wave modulators for 10.6 μm has been investigated. From preliminary experimental results and from theoretical estimates it is concluded that efficient modulators could be constructed in $Hg_{1-x}Cd_xTe$-CdTe waveguides at frequencies up to about 200 MHz, but that the realization of useful modulators at 1 GHz by this technique is doubtful, and the alternative of using bulk acoustic waves should be considered for high-frequency modulators.

# CONTENTS

# INTEGRATED OPTICAL CIRCUITS

## I.  $In_xGa_{1-x}As$-GaAs INTEGRATED OPTICAL CIRCUITS

### A.  SELECTIVE EPITAXIAL DEPOSITION OF $In_xGa_{1-x}As$

Using the growth method described in the first semiannual report,[1] we have integrated small regions of $In_{0.2}Ga_{0.8}As$ into GaAs waveguide structures by the selective epitaxial deposition[2] process shown in Fig. 1.  The waveguide structures in Fig. 1(a) are formed by growing a 5- to 20-μm layer of high-purity ($N_D + N_A \sim 10^{14}$ cm$^{-3}$) GaAs on a heavily doped (n $\sim 10^{18}$ cm$^{-3}$) GaAs substrate using techniques previously described.[3]  Optical guiding can be obtained in the high-purity n-layer since plasma effects reduce the refractive index in the heavily doped n$^+$ substrate.  A pyrolytic $SiO_2$ is then deposited over this waveguide structure, and circular regions are opened in the $SiO_2$ using standard photolithographic techniques.  This patterned $SiO_2$ is then used as an etch mask, and holes are etched through the high-purity layer to the heavily doped substrate to obtain the structure shown in Fig. 1(b).  Depending on the crystallographic orientation and etchant, a variety of hole geometries can be produced.[4]  However, as will be discussed later, the most suitable geometry for a waveguide detector is a hemisphere.  To obtain a hemispherical hole we use a non-preferential etch of 5 $H_2SO_4$ : 1 $H_2O_2$ : 1 $H_2O$ on a {100} surface.  This etchant is allowed to cool for about ten minutes before use to obtain a slower etch rate.

The resulting structure shown in Fig. 1(b) is then placed in the epitaxial reactor, where the $SiO_2$ now serves as a mask against growth.  Thus, epitaxial growth of $In_xGa_{1-x}As$ is obtained only in the holes etched in the GaAs waveguide structure.  The composition of the alloy is graded out to some region, indicated by the dashed line in Fig. 1(c), where the alloy composition is maintained constant at the desired value.  For reasons discussed below, the $In_xGa_{1-x}As$ should be doped to a value at least a factor of five higher than the GaAs waveguide.[5]  Although it would be desirable to terminate growth at the edge of the $SiO_2$, in practice this is somewhat difficult.  Generally, the growth proceeds out of the hole and over the $SiO_2$, giving a faceted structure as indicated in Fig. 1(c).  To obtain the waveguide structure indicated in Fig. 1(d), the $SiO_2$ is removed, and the faceted $In_xGa_{1-x}As$ and the GaAs waveguide are mechanically-chemically polished to the desired thickness with 20 $CH_3OH$ : 1 Br on a rotating pad.

### B.  INTEGRATED $In_xGa_{1-x}As$ AVALANCHE PHOTODIODES

A scanning electron micrograph and a diagram of the upper surface and cleaved cross section of a region of $In_{0.2}Ga_{0.8}As$ grown in a GaAs waveguide structure are shown in Fig. 2.  The faceting indicated in Fig. 1(c) is evident and is typical of that obtained for ⟨100⟩-oriented growth in GaAs[4] as well as $In_xGa_{1-x}As$.  The diameter of the grown-in region is about 125 μm.  The interfaces between the grown-in $10^{16}$ cm$^{-3}$ $In_{0.2}Ga_{0.8}As$, the $10^{14}$ cm$^{-3}$ GaAs waveguide, and the $10^{18}$ cm$^{-3}$ GaAs substrate are delineated by a 1 HF : 3 $HNO_3$ : 4 $H_2O$ etch.  The change in curvature at the interface between the waveguide and the grown-in region, which is undesirable for reasons discussed below, is caused by a slight in situ furnace etch.  The desired structure can be obtained by polishing below this change in curvature.

Figure 3 shows an optical micrograph and a diagram of the cleaved cross section through a similar grown-in region in a 5-μm-thick waveguide.  A Schottky barrier placed over this

hemispherical region of $In_{0.2}Ga_{0.8}As$ and over part of the waveguide surrounding this region produces an essentially ideal detector structure for 1.06-μm radiation propagating through the GaAs waveguide. This structure has the following advantages:

(1) The heavily doped $10^{18}$ cm$^{-3}$ GaAs substrate, in addition to giving the change in refractive index to provide guiding in the $10^{14}$ cm$^{-3}$ GaAs layer, also acts as a closely spaced back contact for a low-resistance, wide-bandwidth device.

(2) The $10^{14}$ cm$^{-3}$ GaAs waveguide also serves as a guard ring[5] for the $10^{16}$ cm$^{-3}$ $In_{0.2}Ga_{0.8}As$ device material, since the reverse-bias breakdown voltage is higher in the lighter doped waveguide material than in the heavier doped detector material.

(3) The hemispherical geometry produces an inverted mesa structure, which reduces the component of electric field along the critical interface region and thereby tends to suppress edge breakdown.[6]

(4) The increased refractive index in the inverted mesa alloy region tends to deflect radiation from the waveguide into the high-field region of the diode.

An SEM photograph of a detector structure fabricated in the way described above is shown in Fig. 4(a). This figure shows the cleaved and stained cross section through a 125-μm-diameter selective epitaxial region of $In_xGa_{1-x}As$ (x ≈ 0.2, n ≈ $10^{16}$ cm$^{-3}$) which was grown in a high-purity (n ≈ $10^{14}$ cm$^{-3}$) GaAs planar waveguide on a heavily doped GaAs substrate. The composition and doping of the selective epitaxial $In_xGa_{1-x}As$ were estimated from absorption edge and Hall effect measurements on an $In_xGa_{1-x}As$ layer grown on an insulating substrate simultaneously with the selective epitaxial growth.

To obtain the structure shown in Fig. 4(a) the $SiO_2$ was removed, and the $In_xGa_{1-x}As$ and GaAs were mechanically-chemically polished to a thickness of about 5 μm. The Schottky barrier detectors were fabricated by first depositing a thin layer of $SiO_2$ over the upper surface and forming an ohmic contact on the n$^+$ GaAs substrate and then photolithographically defining a hole in the $SiO_2$ layer concentric with and slightly larger than the selective epitaxial $In_xGa_{1-x}As$ region. A thin Pt layer was electroplated in this hole to form the Schottky barrier, and additional Au was plated over the Pt for bonding purposes. A photograph of the top view of a finished device is shown in Fig. 4(b). The octagonal outline visible in the Au contact indicates the actual $In_xGa_{1-x}As$ region, and this shape resulted from a slight in situ furnace etch which defined the crystalline planes shown. For electrical and optical evaluation the waveguide structure was mounted on a header, and a Au lead, which is visible in Fig. 4(b), was bonded to the Schottky barrier contact. A schematic cross section of the finished structure is shown in Fig. 4(c).

The reverse bias I-V characteristic of one of the $In_xGa_{1-x}As$ waveguide photodetectors is shown in Fig. 5. The low reverse current and sharp breakdown indicate that the graded interface between the GaAs and the $In_xGa_{1-x}As$ material is of good quality. The estimated bulk breakdown voltage for material with carrier concentration estimated for this device ($\lesssim 1 \times 10^{16}$ cm$^{-3}$) is higher than 50 V while the edge breakdown voltage for a planar Schottky barrier diode would only be about 28 V. The fact that the measured breakdown voltage is approximately equal to the expected bulk breakdown voltage is an indication that the inverted mesa structure and high-purity

GaAs guard ring have reduced the electric field at the perimeter of the device and prevented preferential breakdown in this region.

Since there is only a small dielectric mismatch between the GaAs waveguide and the $In_xGa_{1-x}As$ detector material the quantum efficiency of such a device for the detection of radiation in the waveguide should approach 100 percent for a device of the proper doping and geometry. Specifically, the cross-sectional area of the detector should be large enough to intercept all of the guided radiation in the planar waveguide, or cover the entire cross section of a three-dimensional guide. In addition, the carrier concentration of the $In_xGa_{1-x}As$ should be adjusted so that the detector depletion width is as large as the thickness of the waveguide, and the alloy composition x must be chosen to give relatively high absorption at the desired wavelength of operation.

For optical evaluation, 1.06-$\mu$m radiation from a Nd:YAG laser was coupled into the waveguide using a microscope objective as indicated schematically in Fig. 6. The power incident on the detector was estimated by measuring the radiation transmitted through the planar waveguide when the guided beam was displaced to miss the $In_xGa_{1-x}As$ material and exit through the rear cleaved edge of the sample adjacent to the detector. The losses of these high-purity planar waveguides at 1.06 $\mu$m are less than 1 dB/cm. The quantum efficiency was then estimated using the detector photocurrent, measured when the guided beam was incident on the detector and the estimated power incident on the detector. The value obtained for the quantum efficiency at low bias voltages was 60 percent. This value may have been limited by the relative dimensions of the planar waveguide and the depletion width of this detector. At high reverse bias voltage ($\gtrsim$40V) the external quantum efficiency increases due to avalanche multiplication. Average current gains as high as 50 have been obtained with these devices.

## C. ELECTRON AND HOLE IMPACT IONIZATION COEFFICIENT MEASUREMENTS IN GaAs

The electron and hole impact ionization coefficients ($\alpha$ and $\beta$, respectively) in GaAs are of considerable interest because of their influence on the performance of GaAs avalanche photodetectors and IMPATT diodes. For avalanche photodiodes, the highest gain-bandwidth product and lowest excess noise are predicted when $\alpha$ and $\beta$ are significantly different and the ionization is initiated by the carrier with the higher ionization coefficient. For IMPATT diodes it is generally assumed that the highest conversion efficiency and lowest noise are expected when $\alpha$ and $\beta$ are both large and equal, and if $\alpha$ and $\beta$ are not equal the optimum device structure will depend on their relative magnitudes. GaAs Schottky barrier avalanche photodiodes have been fabricated in which it is possible to achieve nearly pure hole and pure electron injection in the same device. Measurements of the multiplication characteristics of these devices show that the ionization coefficients of electrons ($\alpha$) and holes ($\beta$) are not equal but that $\beta > \alpha$. This result is in agreement with the variation of multiplication with bias voltage at different wavelengths observed for standard GaAs Schottky barrier diodes but contrary to the generally accepted belief that $\alpha = \beta$.

For the determination of $\alpha$ and $\beta$ separately, it is desirable to design an experiment in which essentially pure electron and pure hole injection can be obtained in the same device. From photoelectric measurements of the Schottky barrier heights of different metals on n-type semiconductors, it is well known that essentially pure electron injection can be obtained by irradiating a thin metal Schottky barrier with radiation of energy h$\nu$, $\varphi_B < h\nu < E_g$, where $\varphi_B$ is the barrier height and $E_g$ is the bandgap energy. The same result can be achieved by irradiating the device

from the back through a transparent ohmic contact, in which case the metal Schottky barrier can be opaque. Pure hole injection can be obtained in a Schottky barrier device by shining strongly absorbed radiation, $h\nu > E_g$, through a transparent back ohmic contact so that the minority holes generated optically diffuse to the edge of the depletion and are collected before they recombine. This technique has recently been used for ionization coefficient measurements on Si Schottky barrier diodes.[7]

However, to achieve reasonable hole injection using this method, it is necessary to keep the distance between the edge of the depletion region and the back ohmic contact less than several diffusion lengths. For GaAs these distances are quite small. A schematic drawing of a cross section of the device structure used for the measurements reported here is shown in Fig. 7. The details of the fabrication of this structure will be published in a forthcoming paper.

The multiplication vs voltage curves for holes and electrons [$M_p(V)$ and $M_n(V)$] were determined by measuring the variation of photocurrent with voltage when the diodes were irradiated with 0.633-$\mu$m and 1.06- or 1.15-$\mu$m laser emission, respectively, through the opening in the ohmic contact and ratioing the photocurrent at a given bias voltage to the zero-multiplication photocurrent at the same bias obtained by a linear extrapolation of the low-voltage photocurrents. The electron and hole ionization coefficients, $\alpha$ and $\beta$, were calculated from the multiplication data using the same procedure described in Ref. 7. The results for diodes with net donor concentrations of about $1 \times 10^{16}$ cm$^{-3}$ are shown in Fig. 8. The maximum electric field, $E_m$, covers the range from about $2.5 \times 10^5$ to $3.3 \times 10^5$ V/cm. The ionization rates could not be calculated for $E_m$ below $2.5 \times 10^5$ V/cm because of low multiplication and the stability of experiment. The measurements were terminated at a maximum field of about $3.3 \times 10^5$ V/cm due to possible nonuniformities in the electric field (and hence the multiplication) across the active area of the devices. The scatter in the calculated points is due mainly to the numerical differentiation of the experimental data. Some of the previous ionization coefficient results [8-10] are also shown in this figure for comparison.

There are at least four possible sources of contamination of the injected photocurrents. However, it can be shown that these sources are either insignificant or do not affect the conclusion that $\beta > \alpha$. Before the ultimate performance of GaAs avalanche and IMPATT diodes can be determined, it will be necessary to obtain data for higher fields and higher temperatures. We are presently extending these measurements to devices with higher and lower carrier concentrations to cover a wider field range and to abrupt p-n junctions where we will be able to more accurately account for some of the possible errors mentioned above.

D.  GaAs ELECTROABSORPTION AVALANCHE PHOTODIODE (EAP) DETECTORS

We have observed a new mode of operation of GaAs avalanche photodiodes fabricated on lightly doped n-type material. In contrast to GaAs detectors fabricated on material with $N_D - N_A \approx 10^{16}$ cm$^{-3}$, which have only a very small response at the 0.905-$\mu$m wavelength of room-temperature GaAs lasers, these new EAP detectors have their maximum response at just this wavelength. The absorption at wavelengths below the band edge is due to the Franz-Keldysh effect associated with the electric field in the depletion region of the diode. This "electroabsorption" causes the generation of electron-hole pairs and results in nearly pure hole injection into the avalanche region. Because the ionization coefficient of holes is larger than that of electrons, as discussed above, this mechanism should result in a low-noise device for the detection of GaAs room-temperature laser emission. We are currently investigating the performance of these devices and attempting to integrate them in high-purity GaAs waveguides for use at 0.905 $\mu$m.

## II. $Hg_{1-x}Cd_xTe-CdTe$ INTEGRATED OPTICAL CIRCUITS

### A. EPITAXIAL GROWTH OF $Hg_{1-x}Cd_xTe$ ON CdTe SUBSTRATES

Our initial attempts to develop an epitaxial $Hg_{1-x}Cd_xTe$ capability have been centered around an elemental-source reactor, which is shown schematically in Fig. 9, and growth has been obtained over a range of source and growth temperatures: mercury at 270 to 300°C, cadmium at 360 to 400°C, tellurium at 580 to 650°C, and CdTe seeds at 560 to 600°C. Typical hydrogen flow rates over the sources were 120, 20, and 60 ml/min. for the mercury, cadmium, and tellurium, respectively. With these conditions, growth on CdTe {100}, {110}, {111} Cd, and {111} Te surfaces has been examined, and {100} surfaces have given the best layers from a structural point-of-view. The other surfaces exhibit pronounced effects of constitutional supercooling due to the large segregation of mercury in this system. Because of this problem other techniques are also being investigated.

Layers grown on semi-insulating CdTe substrates have been characterized by resistivity and Hall measurements, electron microprobe analyses, and photoconductivity measurements to obtain carrier concentration and mobility, alloy composition, and energy gap, respectively. Generally, the layers have been n-type with Hall coefficients from 20 to 100 $cm^3/C$. Room-temperature mobility values have increased from about $2.0 \times 10^3$ to $2.5 \times 10^4$ $cm^2/V$-sec with increased HgTe composition. These values are comparable with results obtained on bulk material of similar composition, and the epitaxial layers appear to be of good quality.

Up to the present time we have been able to grow single crystal layers of $Hg_{1-x}Cd_xTe$ over the alloy composition range from $x = 0$ to $x = 0.98$, on CdTe substrates with growth rates as high as 1 µm/min. This should give us sufficient versatility to fabricate a variety of device structures for our ultimate applications. We are currently investigating doping, electrical and compositional uniformity, and selective growth capability to achieve these structures.

### B. CdTe n/n⁺ WAVEGUIDES

#### 1. Materials Characterization

Most of the n-type CdTe used for the fabrication of the 10.6-µm optical waveguides was grown at Lincoln Laboratory by a modified Bridgman technique, using either bromine, indium, or gallium as the dopant. Carrier concentrations as high as about $2 \times 10^{18}/cm^3$ can be obtained with bromine and indium, whereas the donor concentration saturates at about $4 \times 10^{17}/cm^3$ with gallium percentage in the melt.[13] The as-grown wafers were annealed in a Cd atmosphere to remove any possible compensating stoichiometric defects.

The performance of waveguides formed by decreasing the carrier concentration (hence increasing the dielectric constant) near the surface of a CdTe wafer will depend on some degree upon the carrier concentration uniformity of the starting material. It is therefore necessary to examine the homogeneity of the CdTe wafers before fabrication of waveguide structures. Two methods were used to measure the carrier concentration homogeneity of the wafers, Schottky barrier capacitance measurements and free-carrier absorption measurements at 10.6 µm. Both measurements also give the magnitude of the carrier concentration which can be compared with Hall effect data.

The Schottky barrier method involves chemically etching the surface of the CdTe wafer in a 1% bromine-methanol solution and electroplating an array of gold pads onto the surface. Typically,

a pattern of 10-mil squares on 20-mil centers was used. The zero-bias capacitance of the Schottky barriers formed by these gold pads is directly related to the donor concentration in the carrier depletion region. A measurement of capacitance as a function of bias voltage gives the concentration at the end of this depletion region. For donor concentrations above $1 \times 10^{17}/cm^3$ the zero-bias depletion width is less than 0.2 μm. Thus, this method gives information only for a region very close to the surface.

The bromine-doped wafers examined generally exhibited uniform surface concentrations. Typical capacitance variations were ±2 percent over an area of 1 $cm^2$, corresponding to a carrier concentration variation of ±4 percent. A sharp drop in carrier concentration was observed within one or two millimeters of the outside surface of these bromine-doped ingots. Since this portion of the ingot was not used for devices, its presence did not present a serious problem.

Free-carrier absorption measurements at 10.6 μm have been found to provide a simple, nondestructive means of determining the magnitude and homogeneity of the carrier concentration of n-type CdTe wafers doped in excess of $10^{17}/cm^3$. The transmission of a $CO_2$ laser beam is directly related to the average free-carrier density in a volume given by the laser beam diameter and the wafer thickness. In the limit of small transmission, the transmission is given by

$$T = (1 - R)^2 \exp(-\alpha x) \quad ,$$

where R is the reflectivity, $\alpha$ is the free-carrier absorption coefficient, and x is the wafer thickness. Note that for large $\alpha x$ the transmission is not only small, but also extremely sensitive to the value of $\alpha x$. Since $\alpha$ is approximately a linear function of carrier concentration, the $CO_2$ laser transmission profile of a wafer will greatly magnify any carrier concentration inhomogeneities. Obviously, the larger the value of $\alpha x$ the greater the magnification of these inhomogeneities. However, at some point the transmission becomes so small that detector noise becomes a problem. We found that with a pyroelectric detector the optimum transmission level was about $10^{-4}$, which gave us a sensitivity of about 0.1 percent in detectable variation in carrier concentration.

A good approximation to the experimental 10.6-μm free-carrier absorption data in CdTe at room temperature[13] is given by

$$\alpha = 13.5 \, (N/10^{17})^{1.3} \, cm^{-1} \quad ,$$

where N is the carrier concentration in $cm^{-3}$. From this expression an optimum wafer thickness for a homogeneity scan can be determined. For example, a 1-mm wafer thickness can be used to examine wafers with $2 \times 10^{17} < N < 5 \times 10^{17}/cm^3$, whereas a 0.5-mm thickness is useful for $3 \times 10^{17} < N < 9 \times 10^{17}/cm^3$. The wafer thickness was chosen on the basis of Hall data.

$CO_2$ laser transmission scans across two bromine-doped wafers are shown in Figs. 10(a) and 10(b). The wafer in Fig. 10(a) was cut at an angle of about 30° with respect to the growth axis and scanned in that direction. The order-of-magnitude decrease in transmission along the 3.5-cm scan corresponds to only a 30-percent increase in carrier concentration over the 1.8 cm of growth. Distinct, somewhat periodic, variations in transmission are readily apparent, despite the fact that they represent only a few percent variations in carrier concentration. The cause of these fluctuations is yet to be determined. They are not observed, however, when a wafer is scanned in the growth plane, as shown in Fig. 10(b). Here, there is a smooth carrier concentration variation from one side of the wafer to the other. The small bump at the 2.8-cm position is a manifestation of a twin plane and may not represent an actual drop in carrier concentration.

No change in carrier concentration has been observed at grain boundaries. A grain boundary was present at the 1.2-cm position in the wafer of Fig. 10(b). The scan in Fig. 10(a) did not cross any grain boundaries.

The high sensitivity of the probing technique tends to mislead one as to the uniformity of these crystals. Note the 1-cm region in Fig. 10(b) between the 1.5- and 2.5-cm positions has a uniformity of better than ±0.5 percent. Such uniformities are extremely difficult to obtain in any type of crystal. Preliminary data on gallium-doped ingots where the donor concentration saturated at about $4 \times 10^{17}/cm^3$ have indicated better overall uniformity than in these bromine-doped samples. Some difficulty has been encountered in our initial attempt to obtain single crystal regions larger than $1 \ cm^2$ with gallium as the dopant.

Determination of carrier concentration homogeneity by $CO_2$ laser free-carrier absorption scanning is not limited to CdTe. It can be used with any heavily doped semiconductor, n-type or p-type whose energy gap is larger than 0.12 eV. Since free-carrier absorption increases at least as rapidly as $\lambda^2$, a longer wavelength laser might be practical for examining more lightly doped wafers. The nondestructive nature of this technique, the fact that wafer preparation requires only a routine polishing of the surfaces, and the potentially rapid examination rate suggest that free-carrier absorption scanning could become a useful tool for routinely evaluating silicon wafers prior to fabrication of large-area devices (e.g., LSI's, CCD's, or vidicons), where high yield is extremely important. It has certainly proved to be a powerful means of examining CdTe material for use in IOC's and is also being used to evaluate $Pb_{1-x}Sn_x Te$ for similar applications.

2. CdTe n/n$^+$ Waveguide Fabrication and Evaluation

High-energy proton bombardment has been used to produce low-carrier concentration, slab-type optical waveguides at 10.6 μm in heavily doped n-type CdTe.[14] Measured attenuation of such waveguides has been in good agreement with the calculated propagation loss resulting from free-carrier absorption of the evanescent wave penetrating into the high carrier density region beneath the low-concentration bombarded layer. These waveguides have shown propagation losses less than 1 dB/cm and have been uniform to better than ±0.5 dB/cm over a 2-$cm^2$ area.

Prior to the room-temperature proton bombardment, the CdTe wafers were lapped to a thickness of about 0.5 mm and then chemically-mechanically polished with a 1% bromine-methanol solution to obtain a smooth, damage-free surface. A dose of $10^{16}$ monoenergetic protons/$cm^2$ was used to make each waveguiding layer and left a residual free-carrier density of less than $10^{15}/cm^3$, i.e., less than 1 percent of the pre-bombardment value. Proton energies ranging from 0.8 to 2.0 MeV were used to produce guide layers 11 to 40 μm thick. The thickness of the bombarded layer was determined by Schottky barrier capacitance measurements,[14] by occasional cleavage irregularities emanating from the interface between the bombarded layers and the substrate, and by various waveguide properties. These agreed well with values from Janni's tables[14] which give a range varying as the 1.52 power of the proton energy for $0.8 < E_p < 4$ MeV.

The interface between the bombarded layer and the substrate material should be extremely flat, independent of position along the wafer, since the protons have a well-defined average range. In the energy region of 0.8 to 4 MeV the standard deviation about the average range is less than 3 percent, i.e., less than 1 μm for a 30-μm range. The interface should be much smoother than this, since to make the waveguide layer, a very high density of protons is used, over $10^9$ protons in an area corresponding to an optical wavelength squared.

7

The number of modes supported by a given waveguide structure is determined by the guide layer thickness and the difference in refractive index between that layer and the substrate. For waveguides produced by a large, abrupt change in carrier concentration, the carrier concentration of the more heavily doped region is the determining factor. A one-order-of-magnitude decrease in carrier concentration in the bombarded region gives essentially the same mode structure as a four-order-of-magnitude decrease. Thus, the precise concentration of the bombarded layer is not important, and can be assumed to be zero for waveguide mode calculations.

The reduction of the refractive index due to free carriers is somewhat less in CdTe than in GaAs (Ref. 15) due to the larger electron effective mass in CdTe. This decrease in the CdTe refractive index at 10.6 $\mu$m is given by $\Delta n = N/5.9 \times 10^{18}$, e.g., for $N = 1 \times 10^{18}/cm^3$, $\Delta n = 1/5.9 = 0.17$. This relationship was used to calculate[16] the minimum substrate carrier concentration needed to support the various TE waveguide modes as a function of the guide layer thickness as shown in Fig. 11. The corresponding TM modes have slightly higher minimum carrier concentrations. Note that with a substrate concentration of $1 \times 10^{17}/cm^3$, a 20-$\mu$m-thick waveguide is single mode, whereas at $1 \times 10^{18}/cm^3$ this thickness supports four modes.

Waveguide attenuation was determined in two different ways. The first method involved simply focusing the $CO_2$ laser beam onto the cleaved end face of the waveguide and measuring the throughput as schematically illustrated in Fig. 12. An example of the data obtained is shown in the inset, where a peak throughput of 37 percent was observed when the 1-cm-long waveguide was scanned through the laser beam focus. The measured 35-$\mu$m halfwidth agrees well with the calculated 37-$\mu$m range of the 2.0-MeV protons used to fabricate the waveguide. The measured 4.3-dB insertion loss is made up of three contributions: (1) reflectivity loss at the end faces (2.0 dB), (2) coupling loss into the guide, and (3) waveguide attenuation. By examining guides of different lengths the latter two contributions can be separated.

Examination of the far-field pattern of the radiation emanating from the end of the waveguide has provided information on the type of mode propagating down the guide. A typical far-field pattern is shown in Fig. 13. Only a single nearly symmetric lobe is observed in the plane perpendicular to the guide, indicating that a single zero-order mode (TE in this case) was coming from the guide. The measured divergence angle agrees well with the calculated proton range. In all waveguides examined, we have not observed any higher order modes in guides excited by the cleaved end-face technique. This is not surprising considering that a single $TEM_{oo}$ mode laser was used to excite the waveguides.

Waveguide attenuation was also determined by the relative signal from a series of equally spaced grating output couplers. These couplers were sputter etched in the CdTe surface using photolithographic techniques to define the pattern. Figure 14 is an electron-micrograph of a cross section of a typical grating. The 5.08-$\mu$m periodicity gave air-to-waveguide forward coupling at an angle of incidence of about 40° for $TE_o$ modes. The coupler strips, consisting of 50 periodic sections, were spaced 1 mm apart. Variations in output coupling efficiency from strip to strip made it difficult to obtain very precise attenuation values, particularly when the attenuation was small.

The large free-carrier absorption in heavily doped CdTe suggests that absorption of the evanescent wave penetrating into the $n^+$ substrate region may be the dominant attenuation process of the propagating waveguide modes. Such loss can be readily calculated by assuming the attenuation in the substrate does not significantly alter the waveguide parameters (i.e., loss per wavelength is small). Treating the absorption as a perturbation on the mode propagation yields

the following expression for waveguide attenuation

$$\alpha_g = \alpha_s \frac{n_s}{n_g} \frac{P_s}{P_t} \quad , \tag{1}$$

where $\alpha_s$ is the substrate free-carrier absorption coefficient, $n_s$ is the substrate index, $n_g$ the effective guide index, $P_s$ the power in the substrate, and $P_t$ the total power. Using the notation of Tien and Ulrich,[16] for TE modes

$$\frac{P_s}{P_t} = \frac{1}{p_2}\left(\frac{b_1^2}{b_1^2 + p_2^2}\right)\bigg/\left[W + \frac{1}{p_2} + \frac{1}{p_o}\right] \quad , \tag{2}$$

where $p_2$ is the penetration coefficient into the substrate, $p_o$ is the penetration coefficient into the superstrate (generally air), $b_1$ is the component of the wavevector in the guide layer perpendicular to the direction of propagation, and $W$ is the guide layer thickness. The term in the square brackets is the effective waveguide thickness. For TM modes Eq. (1) also holds, but the expression for the power ratio is slightly more complicated.

Calculated waveguide attenuations as a function of waveguide thickness are shown in Fig. 15 for $TE_0$, $TE_1$, and $TM_0$ modes. $TE_0$ attenuation is shown for substrate carrier concentrations of $1 \times 10^{17}/cm^3$ and $2 \times 10^{18}/cm^3$. Although the loss is somewhat less for the more heavily doped substrates, it is not a strong function of substrate concentration. The increased free-carrier absorption with carrier concentration is slightly more than offset by reduced penetration of the evanescent wave. Also note that the $TM_0$ and $TE_0$ losses are very nearly equal. This is the case for the higher order modes also, which is in direct contradiction to previous substrate loss calculations.[15] The $TE_1$ mode has a calculated attenuation four to five times that of the $TE_0$, and the $TE_2$ attenuation is two to three times that of the $TE_1$. Such strong attenuation of higher order modes has the effect of suppressing these modes and making the waveguide essentially single mode, even for the heavily doped substrates. The calculations show that the $TE_0$ and $TM_0$ loss can be quite small, ~5 dB/cm for 21-μm-thick layers and only 1 dB/cm for 39-μm layers.

The data points shown in Fig. 15 were obtained by the methods discussed above. The data plotted represent both $TE_0$ and $TM_0$ modes; as we were unable to detect any difference in loss for the two polarizations. The excellent agreements with the calculated loss strongly suggests free-carrier absorption as the dominant waveguide loss process. Thus, any attenuation due to absorption and scattering in the bombarded layer appears to be much less than 1 dB/cm and consequently unimportant for guides less than 30 μm thick.

Waveguides made by proton bombardment have been quite uniform, as indicated by Fig. 16, where the insertion loss profile of a slab waveguide 21 μm thick and 19 mm long is shown. The average insertion loss was approximately 13 dB, about 4 dB of which was a result of the natural reflectivity of the cleaved end faces and input coupling with an f/3 lens. Over most of the 8-mm scan region, the variation was less than ±1 dB. The region indicated by the sawtooth had a very ragged cleavage on one of the end faces which was probably responsible for the ≈2-dB additional loss in that location. Indeed, small cleavage steps were present over most of the end-face regions and could well have been responsible for all of the observed insertion loss variation.

## C. SCHEMES FOR COUPLING TO CdTe $n/n^+$ WAVEGUIDES

Efficient coupling of a $CO_2$ laser beam into the waveguide structure is a necessary condition for a practical 10.6-μm integrated optical circuit. The high absorption in the $n^+$ substrate region

precludes schemes which involve coupling through the substrate, e.g., the tapered end-fire technique. The ultimate goal of placing a $Hg_{1-x}Cd_xTe$ detector in the waveguide which requires cryogenic operation, makes prism couplers quite difficult to implement because of differential thermal expansion problems. We have therefore concentrated on two coupling schemes: (1) focusing onto a cleaved end face, and (2) sputter-etched grating couplers. The cleaved end-face technique, which is the most direct approach, has been by far the most successful with typical coupling efficiencies of over 70 percent.

We have found that with a 25-mm focal length germanium meniscus lens, a typical 6- to 10-mm-diameter Gaussian laser beam can be routinely coupled through a cleaved end face of a 30-$\mu$m-thick $n/n^+$ CdTe waveguide with a coupling efficiency in excess of 70 percent. In fact, for the 1-cm-long waveguide shown in Fig. 12, the major contribution to the 4.3-dB insertion loss was the 21-percent natural reflectivity at each of the end faces. This loss could, of course, be eliminated by an appropriate antireflection coating.

The cleaved end-face coupling method is particularly well suited for these single-crystal CdTe waveguides which can be cleaved quite smoothly along any $\langle 110 \rangle$ plane. With a $\langle 100 \rangle$ wafer orientation, radiation can be coupled into the guide at any one of the four perpendicular $\langle 110 \rangle$ faces. Although diffraction would indeed make it difficult to couple into guides much less than 20 $\mu$m thick, it presents no problem with the $n/n^+$ CdTe waveguides which must be this thick to avoid excessive free-carrier loss.

Since both cross-sectional dimensions of the optical beam are reduced with a spherical focusing lens, the cleaved end-face technique provides a direct means of coupling into three-dimensional rib or buried waveguide structures. No additional optical components are needed, which would be necessary for the case of prism or grating schemes.

The required translational precision for alignment of the waveguide with respect to the lens is not excessively high. It is about 20 times less than the precision required for waveguides in the visible spectral region. Construction of a rigid lens-waveguide mounting fixture should not be difficult, thus eliminating the need for a micropositioner. The required ±10 $\mu$m translational accuracy would then be converted to a ±0.05° angular alignment accuracy for a 1-cm focal length lens, which is the same type of angular alignment precision necessary for grating and prism couplers. Of course, auto-collimation techniques could be used to make this angular alignment a simple and rapid procedure.

Grating couplers with a 5.08-$\mu$m periodicity have been fabricated into over ten different CdTe waveguides. They are easily etched into the CdTe surface. The 1.7-$\mu$m-deep grooves shown in Fig. 14 were produced by a 90-minute sputter-etch at a power level of only 0.4 W/cm$^2$ using a photoresist mask. Conformable glass photomasks[17] were used to obtain large-area optical contact with the CdTe surface and to insure the integrity of the pattern from one grating coupler pad to another. Grating strips with 50 periodic sections were designed as weak output couplers for use in measuring waveguide attenuation. For coupling into the waveguides, 2.5 × 2.5-mm grating pads with 500 grooves were etched into the surface.

The measured grating input coupling efficiency in most cases was very low. Our best value of about 15 percent for a $TE_1$ mode was obtained with the 21-$\mu$m-thick waveguides. The maximum $TE_0$ efficiency was about 5 percent. From the strength of the output beam we estimated the optimum $TE_0$ coupling length for our strongest coupler (1.7-$\mu$m-deep grooves) to be about 1 cm, which is consistent with theoretical predictions.[18,19] As expected, much weaker coupling was observed for the thicker waveguides. These results are similar to those obtained by other workers.[15]

Competition between the desired input radiation mode and other allowed radiation modes severely limits the efficiency of a grating coupler which is excited from the air interface. Exciting the grating from the substrate, where only one radiation mode couples to the guided mode, is the best approach and can result in efficiencies near the 81-percent theoretical limit.[18,19] With an optimum grating design, that $TE_o$ coupling efficiency when excited from the air interface would be only about 30 percent.[19] Of course, attaining this efficiency requires an input beam diameter equal to the optimum coupling length. The optimum coupling length scales roughly as the waveguide attenuation, since both processes involve the evanescent tail of the guided mode. Consequently, the attenuation experienced by the guided wave beneath the grating is more or less independent of waveguide thickness and mode number, and is calculated to be about 3 dB for $2$-$\mu$m-deep gratings on $n/n^+$ CdTe waveguides. Thus focusing onto a cleaved end face appears to be a far better method of coupling radiation into these waveguides.

## D. INTEGRATED ACOUSTO-OPTIC MODULATORS FOR 10.6 $\mu$m

Bragg-type acousto-optic modulation provides a means of generating a single optical sideband which is diffracted away from the unmodulated portion of the optical beam. This could provide a very clean, frequency-offset local oscillator for a $CO_2$ laser heterodyne detection system. For 10.6-$\mu$m radiation, the Bragg scattering condition can be satisfied for frequency shifts as large as 2 GHz. However, the diffraction angle of the sideband varies with frequency, giving the device an inherently small fractional bandwidth. Integrating an acousto-optic modulator into an optical waveguide at 10.6 $\mu$m is quite different from constructing a discrete unit. Although in an integrated system one has a great many design options, one is also faced with many constraints. For example, the acousto-optic modulator need not be made of the same material as the primary waveguiding layer. It could be an evaporated high-index film in which the guided wave enters, is modulated, and returns to the main waveguide. On the other hand, the acoustic beam thickness must closely match the thickness of the waveguide in order to operate efficiently. The use of a single material for the waveguiding and modulation functions is, of course, the simplest approach and should therefore be considered first. One of the objects of our initial program has therefore been to investigate the feasibility of a surface wave modulator in a CdTe waveguide.

The approximate efficiency of a Bragg modulator is given by[20]

$$\eta = \frac{1}{2} \left[ \frac{\pi L}{\lambda \cos \Theta_B} \right]^2 M_2 P_a$$

$$M_2 = \frac{n^6 p_{eff}^2}{\rho v_a^3} \tag{3}$$

where L is the width of the acoustic beam, $\Theta_B$ the Bragg diffraction angle, $\lambda$ the free-space wavelength of the light wave, $P_a$ the acoustic power density, $p_{eff}$ the effective elasto-optic coefficient, $\rho$ the density of the medium, $v_a$ the acoustic velocity, and n the index of refraction of the material. The quantity $M_2$ is a figure of merit which characterizes the material for acousto-optic modulation efficiency.

Of the materials reasonably transparent at 10.6 $\mu$m, tellurium has the highest known figure of merit ($4 \times 10^{-8}$ cm$^2$/W) (Ref. 21) and requires an acoustic power density of about 30 W/cm$^2$ in a 3-mm beam width to obtain 50 percent modulation efficiency. Although the figure of merit for

CdTe has not been measured, it can be readily estimated since elasto-optic coefficients do not vary greatly from one material to another. The effective elasto-optic coefficient is some linear combination of the elasto-optic tensor components and depends upon the particular diffraction geometry.[22] For any given geometry the value of $p_{eff}$ is a maximum for a particular optical polarization. In Table I we list some of the measured values for Te, Ge, GaAs, and some II-VI compounds.[21] These numbers do not necessarily represent the maximum $p_{eff}$ for the materials, as the individual elasto-optic tensor components must be known before that can be determined. Nevertheless, they serve to illustrate the fact that there is not a wide variation in $p_{eff}$, with most materials exhibiting a value within a factor of two of 0.25. It therefore appears reasonable to assume that CdTe will show a $p_{eff}$ between 0.15 and 0.25. Letting $p_{eff} = 0.2$ and using the $\langle 110 \rangle$ longitudinal velocity of CdTe ($v_a = 3.34 \times 10^5$ cm/sec) (Ref. 23), we get $M_2 = 7 \times 10^{-10}$ cm$^2$/W. Thus, a power density of about 1500 W/cm$^2$ in a 3-mm beam width is needed to obtain 50 percent modulation efficiency in CdTe. Such power densities have been obtained with surface acoustic waves in LiNbO$_3$, GaAs, and many other materials. The surface wave power density is limited by elastic nonlinearities which result in the generation of acoustic wave harmonics. The threshold for harmonic generation in general should not differ appreciably from one material to another.

| TABLE I | |
|---------|-----|
| Material | $p_{eff}$ |
| Te | 0.15 |
| Ge | 0.43 |
| GaAs | 0.23 |
| ZnS | 0.13 |
| CdS | 0.14 |
| HgS | 0.44 |
| ZnTe | 0.15 |

The surface acoustic wave most easily generated is the Rayleigh wave which has its energy confined close to the surface, within a penetration depth of about one-half its wavelength. The velocity of the Rayleigh wave depends upon the particular crystallographic orientation and is somewhat smaller than that of the fast shear wave. Since the fast shear wave in CdTe has a velocity of $1.846 \times 10^5$ cm/sec (Ref. 23), we expect the Rayleigh wave velocity to be about $1.6 \times 10^5$ cm/sec. This low velocity increases our estimated figure of merit by over a factor of 8. However, it also means that a 160-MHz Rayleigh wave will have a 10-$\mu$m wavelength. Consequently, the acoustic energy will penetrate about 1/4 of a 20-$\mu$m-thick $n/n^+$ CdTe waveguide, and the efficiency will be reduced by about 1/4.

Excitation of surface acoustic waves is best done with interdigital electrode transducers, which are capable of very high conversion efficiencies. The efficiency of an interdigital transducer is determined by its acoustoelectric radiation impedance,[24]

$$R_a = \frac{4 N_{fp}}{\pi} k_s^2 \left( \frac{1}{2\pi f C_s N_{fp}} \right) \tag{4}$$

where $C_s$ is the capacitance of a single periodic section, $k_s^2$ is the effective electromechanical coupling constant, and $N_{fp}$ is the number of periodic sections. The electromechanical coupling constant for $\langle 100 \rangle$ propagating shear waves with $\langle 011 \rangle$ particle motion is $6.8 \times 10^{-4}$ in CdTe (Ref. 25). The effective surface wave coupling constant is at best only about 1/5 the bulk value.[26] Thus, for 1-mm-long transducer fingers with a 10-$\mu$m periodicity, we get a maximum radiation impedance of only 0.8 ohm. Series resistance of the evaporated metal electrode fingers will generally be much greater than this. Consequently, a simple interdigital electrode transducer on CdTe will not be very efficient. However, it is well known that a layer of a strongly piezoelectric material evaporated over an interdigital transducer can result in very high effective

12

electromechanical coupling constants. With ZnO, values as high as $2.5 \times 10^{-2}$ have been reported which is close to the value of $LiNbO_3$ (Ref. 27). Our first task therefore involved development of techniques for ZnO disposition on CdTe substrates.

Reactive sputtering in a partial pressure of oxygen necessary to deposit ZnO was found incompatible with a bare CdTe surface. To protect the CdTe surface a 1500-Å layer of $SiO_2$ was pyrolytically deposited onto the CdTe before fabricating the metal interdigital electrodes and sputtering the ZnO overlay. Ten finger-pair gold transducers were fabricated onto ⟨100⟩ CdTe wafers using the metal lift-off technique.[17] Then about 3 μm of ZnO was sputtered over the entire wafer and etched away everywhere except for the areas covering the interdigital electrodes. Figure 17 is a photomicrograph showing the end electrodes of one of these overlay transducers. Optical waveguides were formed by proton bombarding the wafer either before or after the transducer fabrication. The room-temperature waveguide formation process allows this flexibility. The high-energy protons easily penetrate the thin transducer structure and produce high-resistance CdTe beneath it, greatly reducing any parasitic capacitance in the device.

Delay lines consisting of two transducers spaced 5 mm apart and aligned along the ⟨011⟩ direction were examined in order to determine the velocity of the CdTe surface wave and the resonant frequency of the transducers. Network analyzer displays of the transducer frequency response indicated a radiation impedance of less than 5 ohm. Examination of the delay lines using RF pulses revealed a resonant frequency of about 180 MHz with a bandwidth of only a few MHz, indicating very low coupling. The insertion loss of the delay lines was quite high, typically 45 dB. Since surface wave attenuation should not be serious at this frequency (provided a leaky surface wave is not being excited due to slight misalignment) the high insertion loss must result from either inefficient transducers or beam steering loss. A surface wave velocity of $1.64 \times 10^5$ cm/sec was indicated from delay time measurements, which is lower than the value of $1.8 \times 10^5$ cm/sec deduced from the transducer resonance frequency. The latter, however, is the velocity with the 3-μm ZnO film and gold electrodes on the surface. Generally, such mass loading slows down the surface wave. Here the much harder ZnO is actually stiffening the surface wave.

We are in the process of evaluating the acousto-optic modulation efficiency of these devices. In doing so we have found that the gold transducer fingers were unable to withstand 100 mW of RF power on a CW basis without melting. The 5000-Å-thick gold fingers were evidently not thick enough to support the RF current. We expect a maximum modulation efficiency with these transducers of about 0.1 percent, limited by the low conversion efficiency of the transducers, their short length (0.5 mm), and the shallow penetration depth of the 180-MHz Rayleigh waves. The development of high-quality sputtered ZnO films on CdTe will greatly improve the transducer conversion efficiency and allow much longer transducer lengths. Based on the maximum acoustic power density of about 1500 $W/cm^2$ that can be reached before the onset of nonlinear effects, a maximum efficiency of about 10 percent can be estimated for 180-MHz modulation with a 3-mm-wide beam and a 20-μm-thick $n/n^+$ CdTe waveguide. For a 1-GHz modulation frequency the efficiency based on this limitation is reduced to 1.8 percent due to a smaller depth of penetration for the acoustic waves. With a $Hg_{1-x}Cd_xTe/CdTe$ waveguide an effective minimum waveguide thickness of about 4 μm may be realizable. For this waveguide the maximum efficiency would be 50 percent at 180 MHz and 9 percent at 1 GHz. In practice, the modulation will probably be limited by the maximum CW power that can be generated by the transducers. Based on this limitation, we can expect 10-percent efficiencies for 4-μm $Hg_{1-x}Cd_xTe/CdTe$ waveguides at frequencies

up to about 200 MHz. For a 1-GHz frequency the transducer radiation impedance will be much lower, and the realization of even a 1-percent efficiency with a 4-μm waveguide seems doubtful.

The use of bulk acoustic waves appears to be the best approach for obtaining a strong sideband signal with a large frequency shift in the $n/n^+$ CdTe waveguides. High-frequency bulk wave transducers can be fabricated onto either semiconducting or semi-insulating CdTe by sandwiching a ZnO film between two conducting metal films.[28] In the case of optical waveguides, this would have to be done on a cleaved end face. A ZnO film 2 μm thick has a longitudinal acoustic wave resonance at 1.6 GHz, and a transducer with a 3-mm by 25-μm cross section should have an acoustic radiation impedance of a few ohms. About 1 W of acoustic power would be needed to give rise to 50 percent sideband conversion. Whether or not this power level can be realized at 1.6 GHz will depend upon the magnitude of the acoustic attenuation in CdTe.

# REFERENCES

1. Integrated Optical Circuits Semiannual Technical Summary, Lincoln Laboratory, M.I.T. (31 July 1973), p. 1, DDC AD-769858/2.

2. B. D. Joyce and J. A. Baldrey, Nature 195, 485 (1962).

3. C. M. Wolfe and G. E. Stillman, Proc. 3rd Int. Symp. GaAs (Inst. Physics, London, 1971), p. 3.

4. D. W. Shaw, J. Electrochem. Soc. 113, 904 (1966).

5. C. M. Wolfe and W. T. Lindley, J. Electrochem. Soc. 116, 276 (1969).

6. D. J. Coleman, Jr., J. C. Irvin and S. M. Sze, Proc. IEEE 59, 1121 (1971).

7. M. H. Woods, W. C. Johnson and M. A. Lampert, Solid State Electron. 16, 381 (1973).

8. R. A. Logan and S. M. Sze, J. Phys. Soc. Japan 21, Supplement, 434 (1966). [Proc. Intl. Conf. Phys. Semicond., Kyoto, 1966].

9. H. Kressel and G. Kupsky, Int. J. Electronics 20, 535 (1966).

10. Y. J. Chang and S. M. Sze, J. Appl. Phys. 40, 5392 (1969).

11. S. N. Shabda and C. Yeh, J. Appl. Phys. 41, 4743 (1970).

12. R. Hall and J. H. Leck, Int. J. Electronics 25, 529 (1968).

13. Solid State Research Report, Lincoln Laboratory, M.I.T. (1972:2), p. 23, DDC AD-748836.

14. Integrated Optical Circuits Semiannual Technical Summary, Lincoln Laboratory, M.I.T. (31 July 1973), p. 5, DDC AD-769858/2.

15. P. K. Cheo, J. M. Berak, W. Oshinsky and J. L. Swindal, Appl. Opt. 12, 500 (1973).

16. P. K. Tien and R. Ulrich, J. Opt. Soc. Am. 50, 1325 (1970).

17. H. I. Smith, F. J. Bachner and N. Efremow, J. Electrochem. Soc. 118, 821 (1971).

18. J. H. Harris, R. K. Winn and D. G. Dalgoutte, Appl. Opt. 11, 2234 (1972).

19. K. Ogawa, W. S. C. Chang, B. L. Sopori and F. J. Rosenbaum, IEEE J. Quantum Electron. QE-9, 29 (1973).

20. C. F. Quate, C. D. Williamson and D. K. Winslow, Proc. IEEE 53, 1604 (1965).

21. N. Uchida and N. Niizeki, Proc. IEEE 61, 1073 (1973).

22. G. B. Benedek and K. Fritsch, Phys. Rev. 149, 647 (1966).

23. H. J. McShimin and D. G. Thomas, J. Appl. Phys. 33, 56 (1962).

24. W. R. Smith et al., IEEE Trans. Microwave Theory Tech. MTT-17, 856 (1969).

25. D. A. Berlincourt, H. Jaffe and L. R. Shiozawa, Phys. Rev. 192, 1009 (1963).

26. J. J. Campbell and W. R. Jones, J. Appl. Phys. 41, 2796 (1970).

27. F. S. Hinkernell and J. W. Brewer, Appl. Phys. Letters 21, 389 (1972).

28. T. M. Reeder and D. K. Winslow, IEEE Trans. Microwave Theory Tech. MTT-17, 927 (1969).

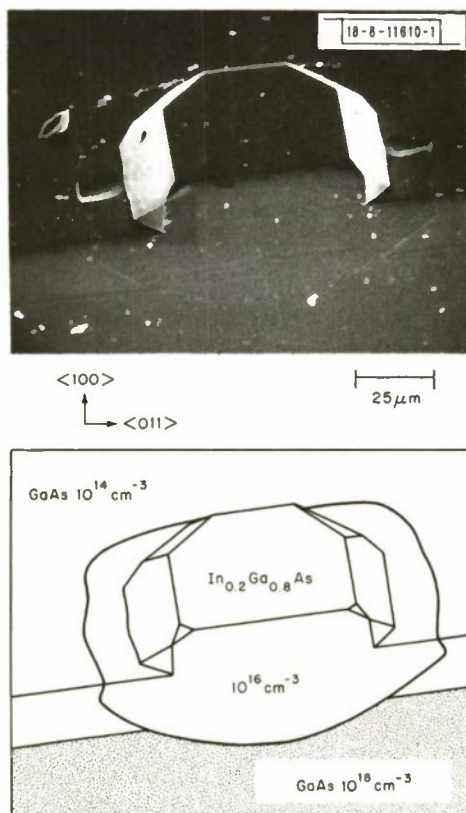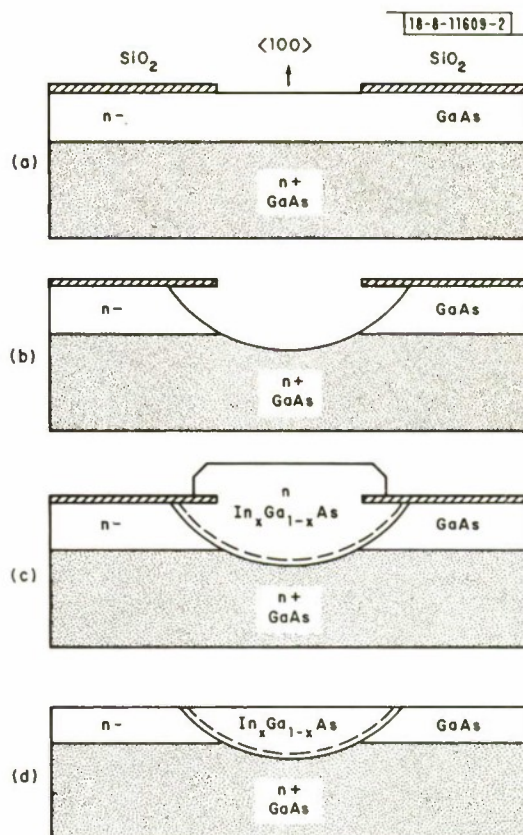Fig. 1. Selective epitaxial deposition process for forming waveguide detector structures.



Fig. 2. Scanning electron micrograph and diagram showing the upper surface and cleaved cross section of an In$_{0.2}$Ga$_{0.8}$As region grown in a GaAs high-purity waveguide.
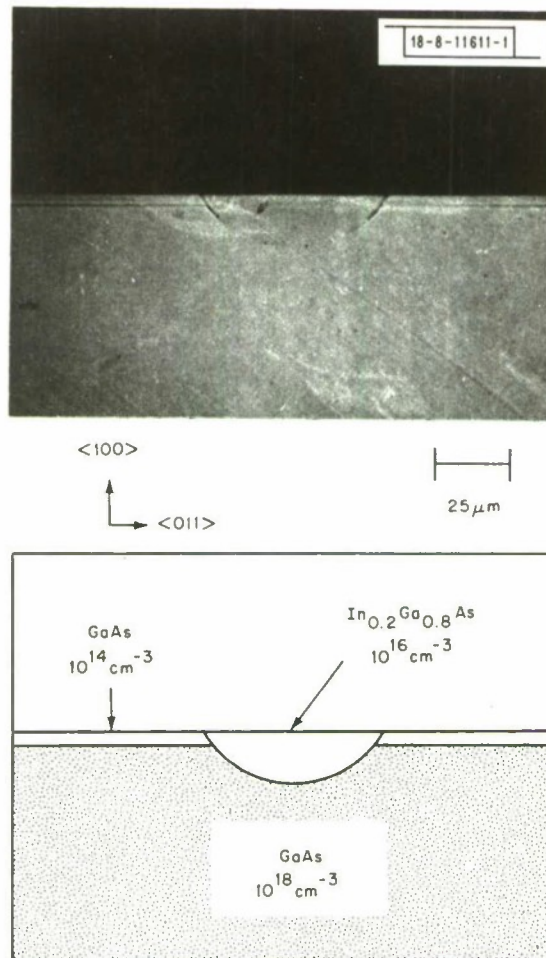
16

<100>

<011>

25 μm

GaAs
$10^{14} cm^{-3}$

$In_{0.2}Ga_{0.8}As$
$10^{16} cm^{-3}$

GaAs
$10^{18} cm^{-3}$

Fig. 3.   Optical micrograph and diagram showing the cleaved cross-section through a waveguide detector structure.

**(a) SEM PHOTOGRAPH**

InGaAs SELECTIVE EPITAXIAL GROWTH

HIGH-PURITY EPITAXIAL GaAs PLANAR WAVEGUIDE

$n^+$-GaAs SUBSTRATE

PT SCHOTTKY BARRIER AND Au PLATING

InGaAs DETECTOR

1.06-$\mu$m RADIATION INCIDENT ON CLEAVED EDGE OF WAVEGUIDE

PLANAR GaAs WAVEGUIDE

**(b) TOP VIEW**

PT SCHOTTKY BARRIER AND Au PLATING

InGaAs

PLANAR WAVEGUIDE

1.06-$\mu$m RADIATION

$n^+$-GaAs

OHMIC CONTACT

**(c) SCHEMATIC DIAGRAM**
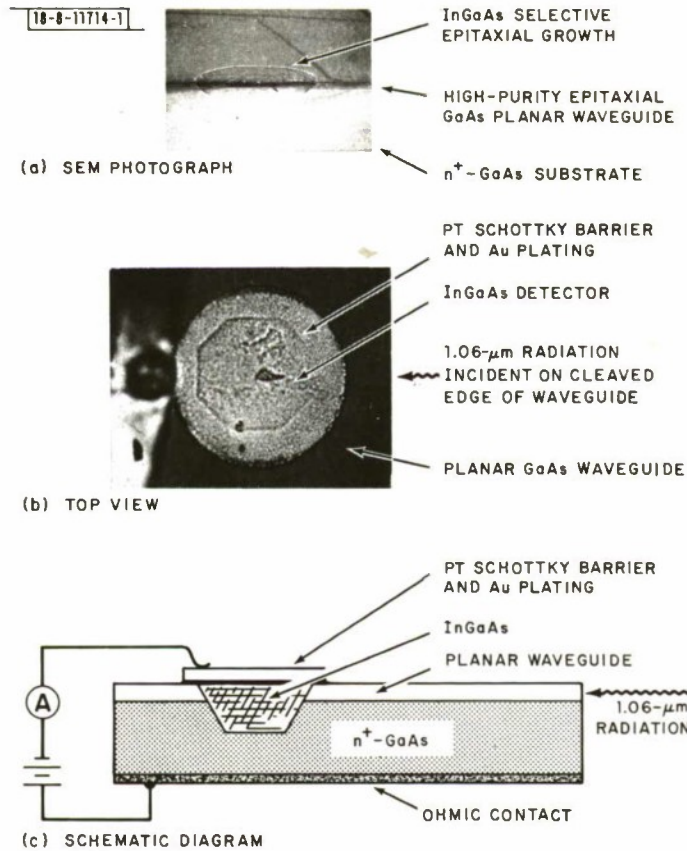
Fig. 4. Structure of monolithic integrated $In_{1-x}Ga_xAs$ waveguide photodetector: (a) SEM cross section, (b) photograph of top view of finished device, (c) schematic cross section of detector-waveguide structure.



20V

10$\mu$A
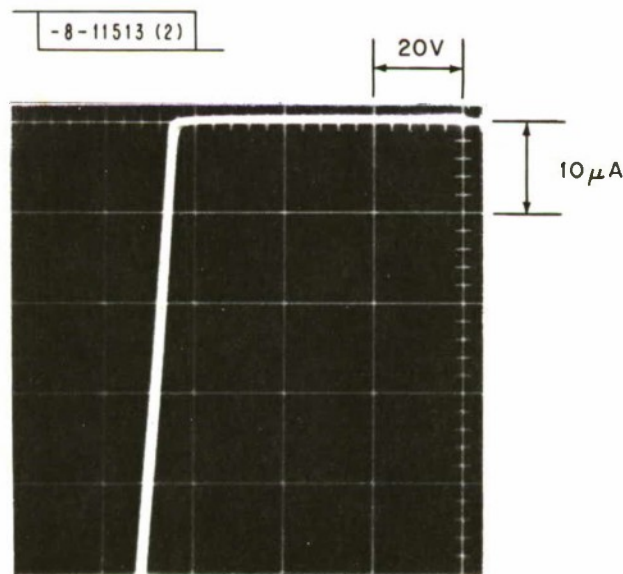
Fig. 5. Reverse bias I-V characteristic of integrated waveguide photodetector.

CLEAVED EDGE

GUIDED BEAM

CLEAVED EDGE

INCIDENT RADIATION
1.06 μm

InGaAs

HIGH-PURITY GaAs PLANAR WAVEGUIDE

n⁺ GaAs SUBSTRATE

Au + Sn OHMIC CONTACT

Pt SCHOTTKY BARRIER + Au CONTACT
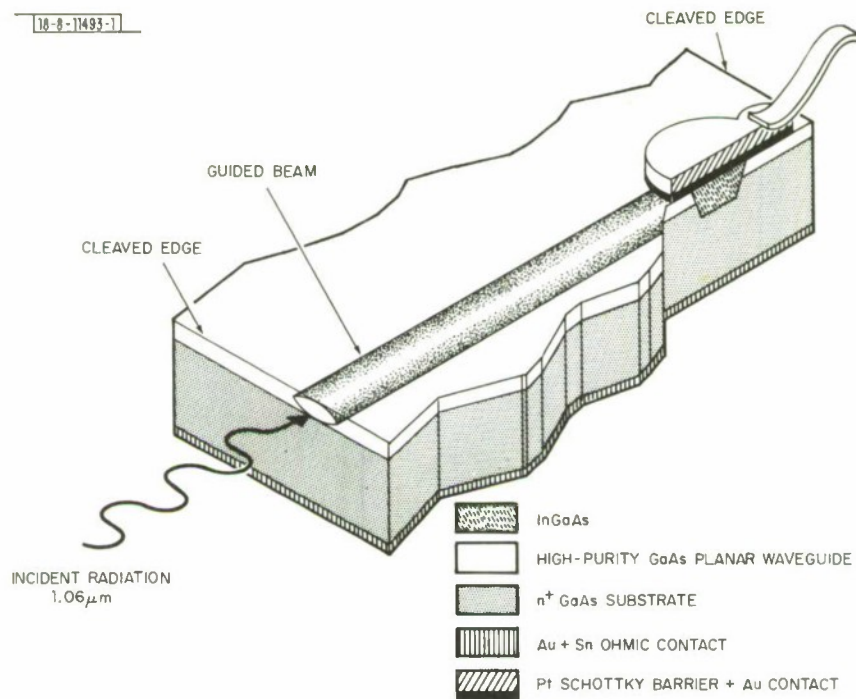
Fig. 6. Schematic cross section of waveguide detector structure showing method used for optical evaluation.

Au

Pt

Al₂O₃

SiON

SiO₂

EPOXY

HIGH-RESISTIVITY GaAs

EPITAXIAL GaAs

Au-Sn + Au OHMIC CONTACT
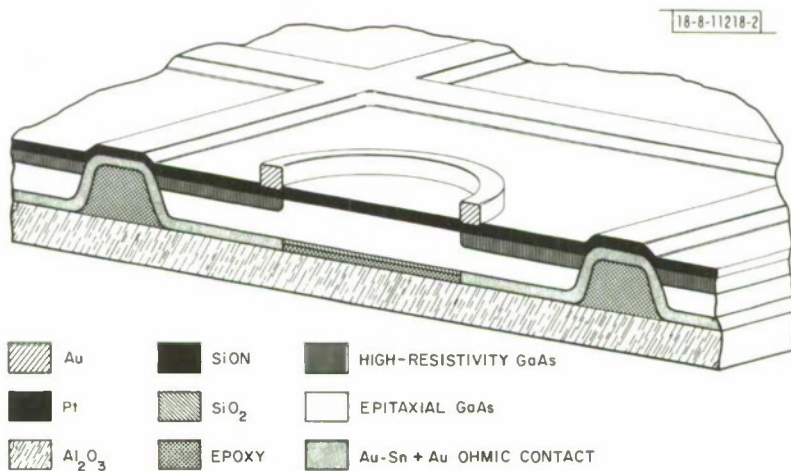
Fig. 7. Device structure used to obtain relatively pure electron and hole injection in the same Schottky barrier device.
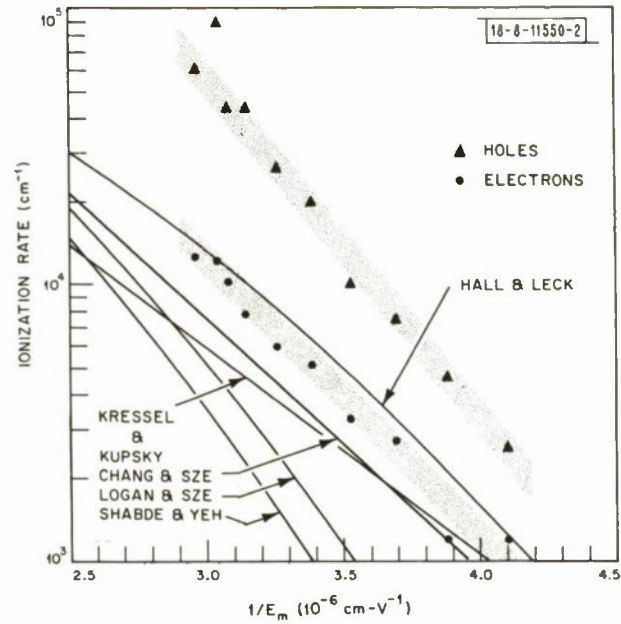
Fig. 8. Experimental field dependence of electron and hole ionization coefficients in GaAs. The curves show the field dependencies determined by some previous workers with the assumption $\alpha = \beta$.
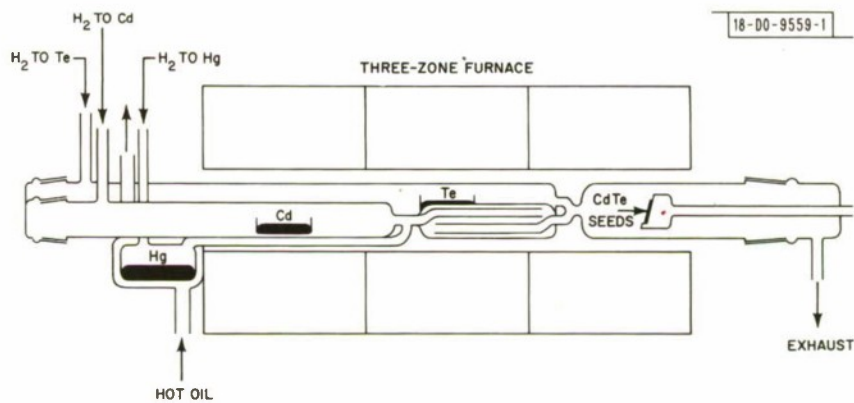


Fig. 9. Epitaxial $Hg_{1-x}Cd_xTe$ growth reactor.
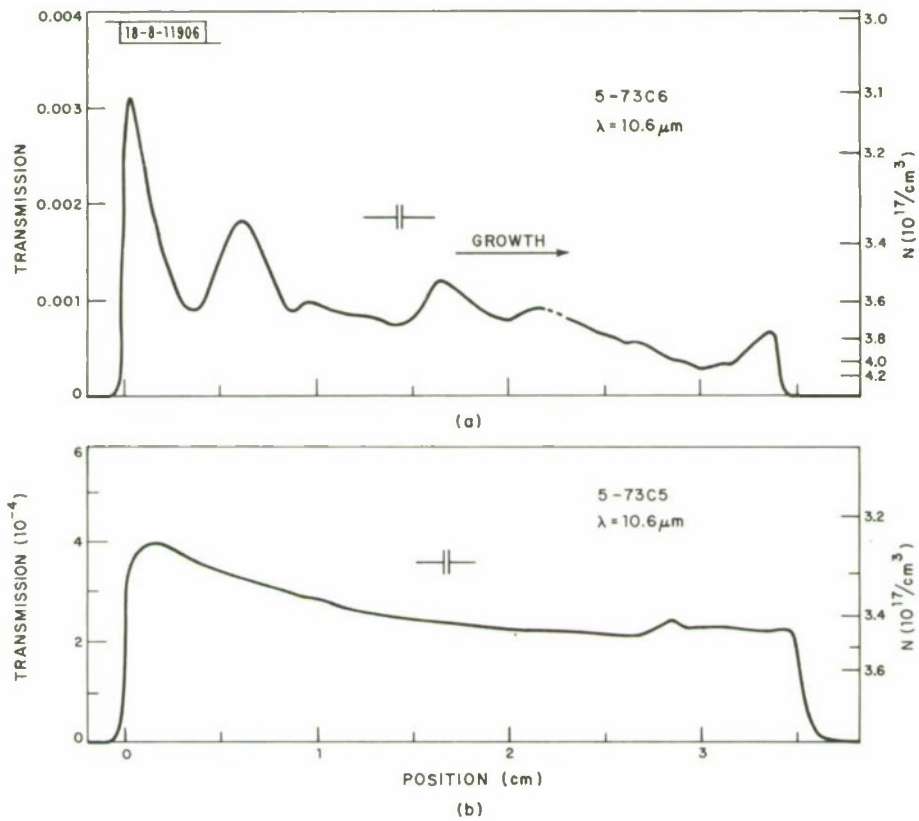
Fig. 10.   CO$_2$ laser transmission profiles across two bromine-doped CdTe wafers.
Profile in (a) is at an angle of about 30 degrees with respect to the growth plane,
whereas profile (b) is in the growth plane.
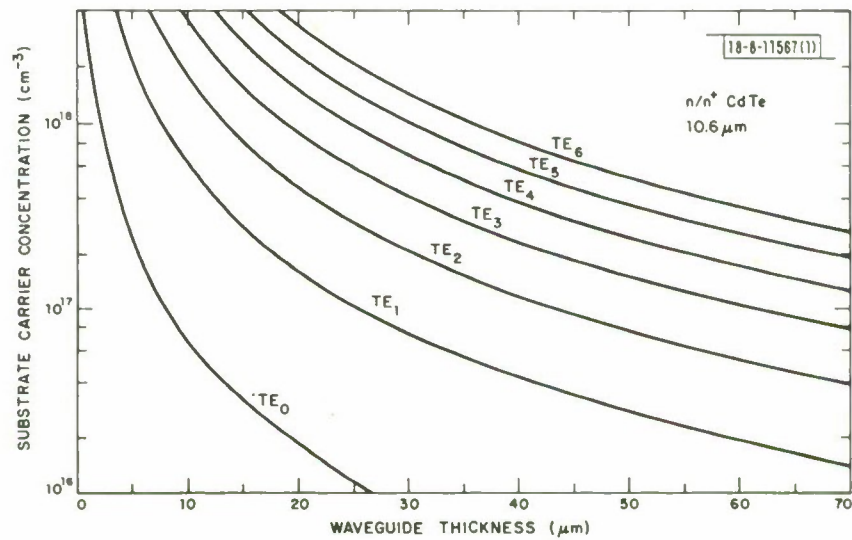


Fig. 11.   Substrate carrier concentration required to support various TE waveguide
modes for the n/n$^+$ CdTe structure as a function of waveguide thickness.

21
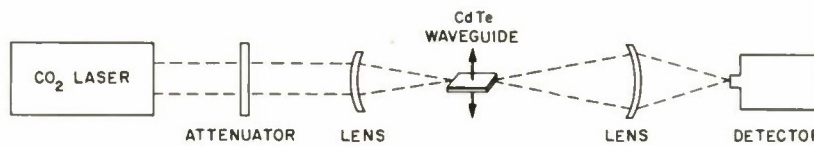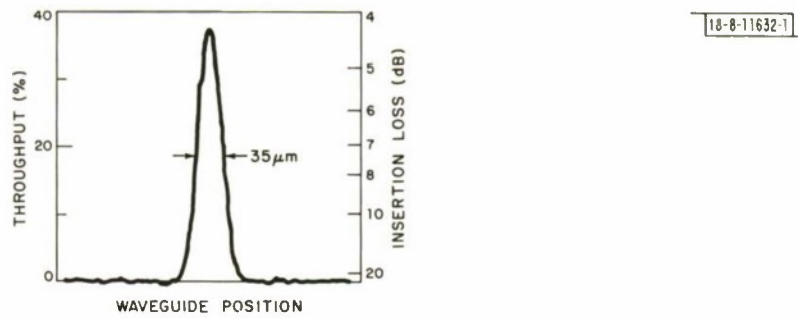
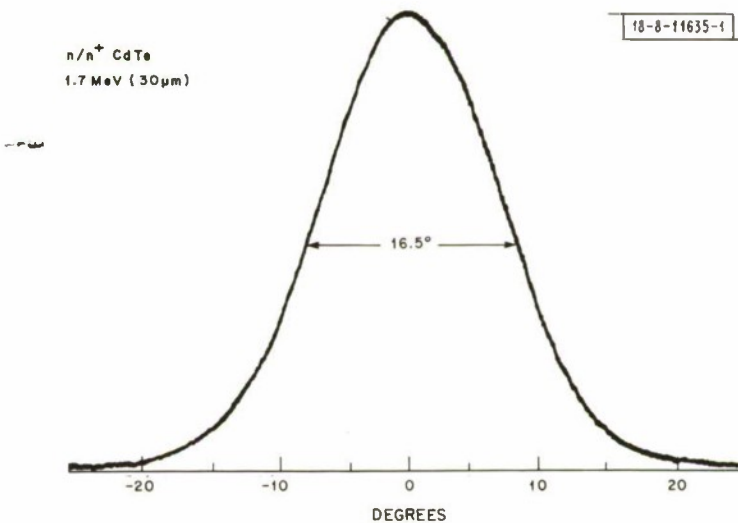Fig. 12.   Experimental setup used to measure waveguide attenuation showing a typical throughput recording.



Fig. 13.   Far-field pattern observed emanating from a waveguide excited by focusing onto a cleaved end face.

Fig. 14. Electromicrograph showing the profile of a sputter-etched grating coupler in CdTe.
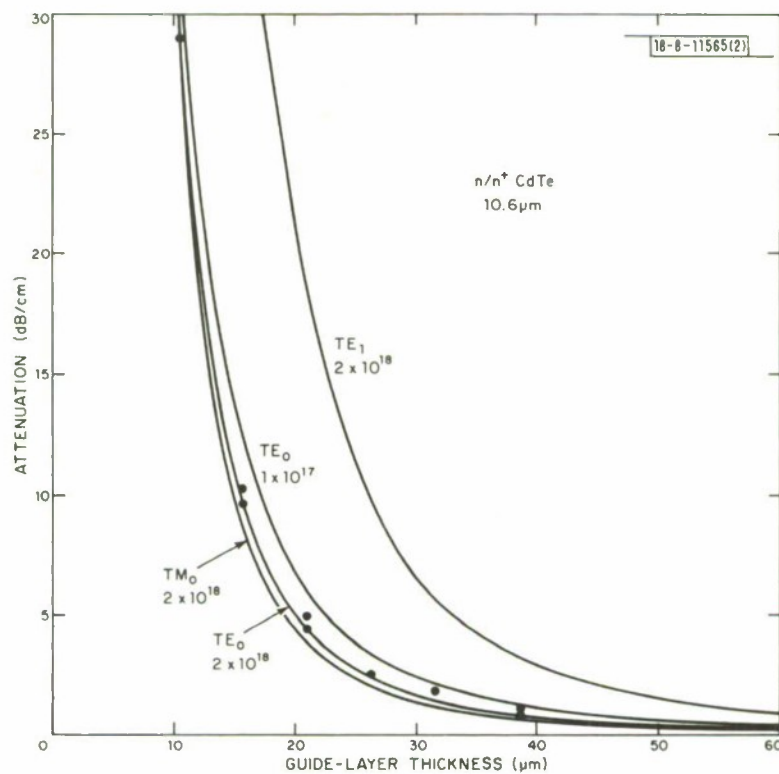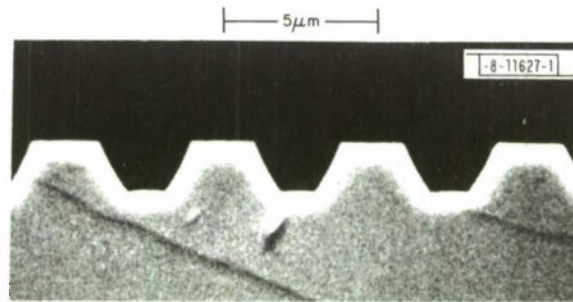


Fig. 15. Measured and calculated n/n$^+$ CdTe waveguide attenuation as a function of guide-layer thickness.
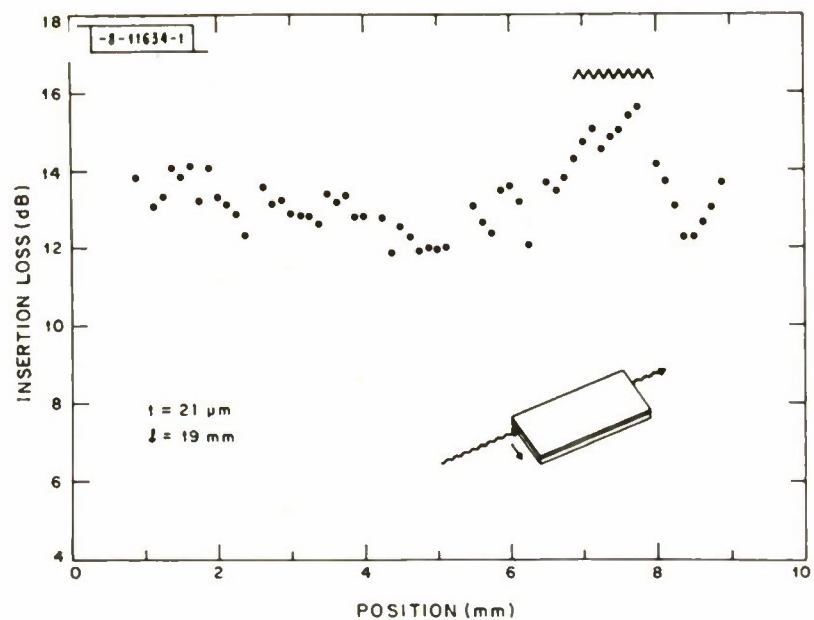
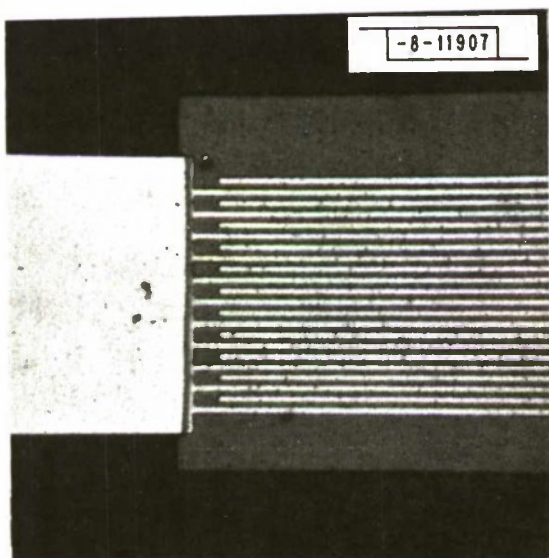Fig. 16.   Insertion loss profile of a 21-μm-thick CdTe slab waveguide.



Fig. 17.   Photomicrograph of a ZnO overlay transducer on CdTe with a 5.08-μm electrode spacing.

| REPORT DOCUMENTATION PAGE | | READ INSTRUCTIONS<br>BEFORE COMPLETING FORM |
|---|---|---|
| 1. REPORT NUMBER<br>ESD-TR-74-172 | 2. GOVT ACCESSION NO. | 3. RECIPIENT'S CATALOG NUMBER |
| 4. TITLE *(ond Subtitle)*<br><br>INTEGRATED OPTICAL CIRCUITS | | 5. TYPE OF REPORT & PERIOD COVERED<br>Semiannual Technical Summary<br>1 July – 31 December 1973 |
| | | 6. PERFORMING ORG. REPORT NUMBER |
| 7. AUTHOR*(s)*<br><br>Wolfe, Charles M.        Spears, David L.<br>Stillman, Gregory E.    Melngailis, lvars | | 8. CONTRACT OR GRANT NUMBER*(s)*<br><br>F19628-73-C-0002 |
| 9. PERFORMING ORGANIZATION NAME AND ADDRESS<br><br>Lincoln Laboratory, M.I.T.<br>P.O. Box 73<br>Lexington, MA   02173 | | 10. PROGRAM ELEMENT, PROJECT, TASK<br>AREA & WORK UNIT NUMBERS<br><br>ARPA Order 2074 |
| 11. CONTROLLING OFFICE NAME AND ADDRESS<br><br>Advanced Research Projects Agency<br>1400 Wilson Boulevard<br>Arlington, VA   22209 | | 12. REPORT DATE<br>31 December 1973 |
| | | 13. NUMBER OF PAGES<br>32 |
| 14. MONITORING AGENCY NAME & ADDRESS *(if different from Controlling Office)*<br><br>Air Force Cambridge Research Laboratories<br>L.G. Hanscom Field<br>Bedford, MA   01730 | | 15. SECURITY CLASS. *(of this report)*<br><br>Unclassified |
| | | 15a. DECLASSIFICATION DOWNGRADING<br>SCHEDULE |

16. DISTRIBUTION STATEMENT *(of this Report)*

Approved for public release; distribution unlimited.

17. DISTRIBUTION STATEMENT *(of the obstroct entered in Block 20, if different from Report)*

18. SUPPLEMENTARY NOTES

None

19. KEY WORDS *(Continue on reverse side if necessary and identify by block number)*

| | | |
|---|---|---|
| Integrated Optical Circuits | epitaxial growth | $Hg_{1-x}Cd_xTe$-CdTe |
| $In_xGa_{1-x}As$-GaAs | heterodyne detection | Schottky barrier |
| vapor-phase system | avalanche photodiodes | proton bombardment |

20. ABSTRACT *(Continue on reverse side if necessary and identify by block number)*

$In_xGa_{1-x}As$ avalanche photodiodes have been integrated into GaAs waveguide structures by selective epitaxial deposition. Measurements of the ionization coefficients of electrons ($\alpha$) and holes ($\beta$) have been made for GaAs by using a special type of GaAs Schottky barrier avalanche photodiode structure. A new type of GaAs avalanche photodiode which has considerable advantages for detection at wavelengths up to $0.93\,\mu m$ has been investigated.

Significant progress has been made in the vapor epitaxial growth of $Hg_{1-x}Cd_xTe$ on CdTe substrates by $H_2$ transport. High-energy proton bombardment has been used to fabricate waveguides for $10.6\,\mu m$ in CdTe. Coupling of $10.6$-$\mu m$ radiation into CdTe waveguides has been explored. The feasibility of integrated surface acoustic wave modulators for $10.6\,\mu m$ has been investigated.

DD FORM<br>1 JAN 73 **1473**   EDITION OF 1 NOV 65 IS OBSOLETE